Analysis of Particle-Stimulated Nucleation (PSN)-Dominated Recrystallization for Hot-Rolled 7050 Aluminum Alloy

KHALED F. ADAM, ZHENGDONG LONG, and DAVID P. FIELD

In 7xxx series aluminum alloys, the constituent large and small second-phase particles present during deformation process. The fraction and spatial distribution of these second-phase particles significantly influence the recrystallized structure, kinetics, and texture in the subsequent treatment. In the present work, the Monte Carlo Potts model was used to model particle-stimulated nucleation (PSN)-dominated recrystallization and grain growth in high-strength aluminum alloy 7050. The driving force for recrystallization is deformation-induced stored energy, which is also strongly affected by the coarse particle distribution. The actual microstructure and particle distribution of hot-rolled plate were used as an initial point for modeling of recrystallization during the subsequent solution heat treatment. Measurements from bright-field TEM images were performed to enhance qualitative interpretations of the developed microstructure. The influence of texture inhomogeneity has been demonstrated from a theoretical point of view using pole figures. Additionally, *in situ* annealing measurements in SEM were performed to track the orientational and microstructural changes and to provide experimental support for the recrystallization mechanism of PSN in AA7050.

I. INTRODUCTION

HIGH-STRENGTH, precipitation-hardening, 7xxx aluminum alloys such as AA7050 are widely used in the aviation industry because they consolidate high-strength, low-density, better stress-corrosion cracking resistance, and stronger fracture toughness.[1–3] AA7050 is one of the best choices for thick part applications such as wing ribs, spars, and fuselage frames.[4] The critical applications of these alloys will necessitate further investigation and development in various areas associated with the thermal processing. The mechanical properties of these alloys are affected by evolved structure (grain size and texture) during recrystallization.[5] Recrystallization reduces strength and toughness and can decrease the corrosion resistance of aged alloys. A small volume fraction of recrystallization is tolerable for structural applications requiring high strength.[6,7] Modeling the microstructural evolution during recrystallization can aid in optimizing the recrystallized fraction for applications and industrial needs.

The production of 7050 aluminum alloys goes through a series of processing stages including casting, homogenization, preheating, hot rolling, solutionizing, quenching, and aging.[1,5] Decomposition and precipitation of second-phase particles can take place during any of the processing stages, which in turn influences the evolving structure of the following stages.[1,5] The spatial distribution of these particles depends on the cooling rate, prior microstructure, and local chemistry composition.[1] S-phases (Al_2CuMg), M-phase, or η-phase $Mg(Zn_2, AlCu)_2$ and T-phase are the most common precipitated phases in 7050 Al alloy, in addition to the insoluble iron and silicon-rich constituent particles that form during ingot solidification.[1,4,8] These particles persist through hot rolling and are hard enough to hamper the metal flow during the hot-rolling process.[4] The stored deformation energy in these regions is high, and high misorientation gradients develop in the vicinity of such particles.[4,9–11]

Unlike much of the published work, the distribution of nucleation sites used as input for the simulations was determined from real experiments obtained from the BSE micrographs.[12] Anisotropy of the subgrain boundary energy was implemented into the Monte Carlo code.[13,14] Nevertheless, adding the Zirconium to add control over the recrystallized grain structure in 7050 aluminum alloys is important. The metastable coherent Al_3Zr dispersoids greatly hinder the recrystallization process.[4–8,15–18] Particles of Al_3Zr pin grain and sub-grain boundaries make grain growth more challenging in areas far from the large particle. These Al_3Zr dispersoids are mainly found in the grain center and less-so in the near grain boundary regions.[18] Furthermore, during non-isothermal annealing of heat treatable aluminum alloys, concurrent precipitation of dispersoids is expected to take place, suppressing nucleation and delays recrystallization.[19]

KHALED F. ADAM and DAVID P. FIELD are with the School of Mechanical and Materials Engineering, Washington State University, PO Box 642920, Pullman, WA, 99164. Contact e-mail: k-adem@wsu.edu ZHENGDONG LONG is with Kaiser Aluminum, 15000 E Euclid Ave, Spokane Valley, WA 99216.

Compared to the experimental research,[20–25] few attempts of computer simulation have addressed the particle-stimulated nucleation (PSN) of recrystallization.[9,11,26] Rad and coworkers[9] have coupled two computational techniques to simulate texture and structure for particle-containing alloys during deformation and subsequent annealing processes. Furthermore, Eivani and colleagues[27] have included the effect of stored energy and Zener pinning in a Monte Carlo algorithm to enhance the accuracy of the predicted model. However, these works were conducted on ideal, computer-generated, structures and did not take the second-phase particle distribution into account. Baudin and colleagues[28,29] have simulated the grain growth started from realistic microstructures.

The current study was envisioned to prove the benefits of integrating the experiment into the simulation model to predict accurately the evolved structure during static recrystallization for the 7050 Aluminum alloy. The Monte Carlo model was used to simulate PSN and grain growth starting during recrystallization. The spatial inhomogeneity of nucleation is obtained from measurement of the actual second-phase particle distribution in the matrix identified using backscattered electron (BSE) imaging. The initial microstructures for the simulations were obtained using electron backscatter diffraction (EBSD) of the same region. The Read–Shockley model was also employed in order to include the realistic textures and disorientation distributions in the Monte Carlo Potts algorithm. The effective driving pressure for recrystallization due to dislocation accumulation around the large particle and the Zener pinning pressure due to the finely dispersed particles in areas far from large particles and grain boundaries were determined using the Gibbs–Thompson formula. Furthermore, *in situ* EBSD experiments have been performed to verify the validity of simulation results and elucidating that PSN is the dominant mechanism of recrystallization in the AA7050 alloy.

The *in situ* experiments in the SEM provide a valuable insight into characterizing the orientation and microstructure evolution during the recrystallization of PSN.[30] *In situ* EBSD have used to different aspects of annealing phenomena such as grain boundary mobility,[31] twin formation,[32] recrystallization and grain growth,[33,34] texture evolution,[35,36] recrystallization mechanism,[37] and phase transformation.[38] Capturing the process of PSN recrystallization in hot-rolled AA7050 alloy, to relate nucleation and growth processes during recrystallization with the deformed microstructure, can help control recrystallization.

II. EXPERIMENTAL DETAILS

A. *Material and Microscopy*

The alloy investigated in this project is a 7050 Al alloy whose nominal composition in (pct wt) was 6.2 pct Zn, 2.3 pct Cu, 2.2 pct Mg, and 0.12 pct Zr with minor amounts of Si, Fe, Mn, Cr, and Ti. Cubic shape samples were cut from a hot-rolled 5-inch-thick plate, provided

by Kaiser Aluminum Company, Spokane WA. The 127 mm 7050 Al alloy plate had been rolled from an ingot of 508 mm initial thickness. For TEM examination, thin foils of 7050 Al alloy approximately 1 mm in thickness were cut using a slow speed diamond saw. A number of 3 mm size disks were punched out from these foils and were mechanically ground and polished down to ~0.5 mm in thickness before being twin-jet electro-polished to suitable thickness for electron transmission in TEM examination. TEM was performed using a Philips CM200 TEM operated at 200 kv. High-resolution SEM was conducted in a field emission gun scanning electron microscopy (FEGSEM) operated at 20 kV. EBSD was carried out using the FEGSEM with scans taken over a square array of measurement. Micro-hardness indentation was used to identify the measurement area for EBSD and BSE. OIM software in combination with Dream3d software was used to post process the simulation output data.[39,40] The imageJ software package was used to threshold the BSE images and to determine the size and area fraction of the large particles.[41] To minimize the effects of noise, all particles smaller than 4 μm ignored. The EBSD and BSE measurements were performed for RD-ND and TD-RD planes of 7050 sample.

B. *Heat Stage Setup*

In situ heating experiments were performed inside the SEM chamber by a heat stage designed to provide the necessary tilts for EBSD measurements as well as to measure and control the sample temperature from outside the SEM (Figure 1(a)). The heating stage used in this work is capable of heating the sample up to 1593.15 K (1320 °C). The samples size was 5 mm × 7 mm × 0.5 mm. Because AA7050 is a non-weldable alloy, the specimen temperature was tracked through thermocouple reading of heating stage itself, and the temperature is expected to be homogenous in such a thin sample. Another challenge is that specimens can gradually move during *in situ* experiments. In addition to the specimen drifting, at high temperatures around 612.15 K (350 °C) the pattern quality decreased and unsuccessfully indexed areas close to large particles and grain boundaries. The samples were heated sequentially in temperatures 298.15 K (25 °C) steps for time intervals of ~10 minutes duration. After each heating step, the surface was mapped using automated EBSD (OIM). The AA7050 specimens documented in this work were heated to ~623.15 K (350°C) (Figure 1(b)).

C. *TEM Observation*

Transmission electron microscope (TEM) was used to characterize the microstructural features that may affect the recrystallization behavior in high-strength alloys, such as precipitate-free zones and dispersoid particles (Al_3Zr). Upon preheating stage, the dispersoids Al_3Zr particles were often found to be spherical with a diameter of 15 to 30 nm.[14] Figure 2(a) is a bright-field TEM micrograph of unrecrystallized structure for AA7050. The pinning particles (Al_3Zr) obviously appear
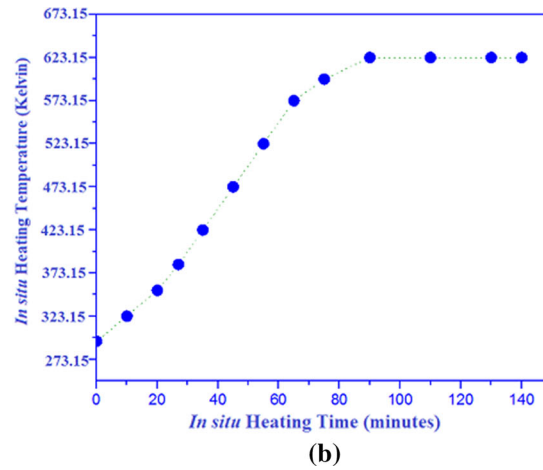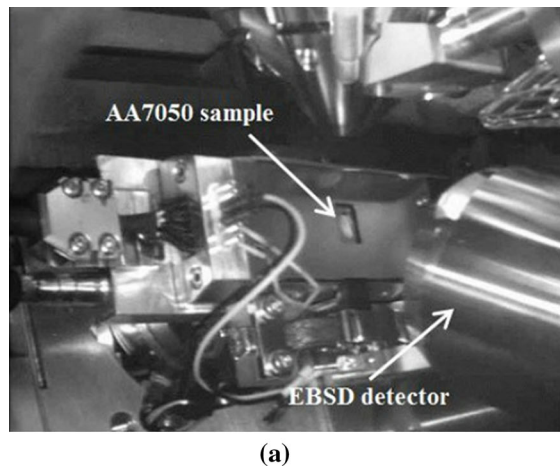
Fig. 1—(a) Heating stage fixed in the SEM chamber, tilted to 70 deg to suit EBSD settings. (b) Data from thermocouple measurements at heating surface inside the furnace.

as dark spots randomly distributed in the interior of the grains. These nano-size particles act as recrystallization inhibitors so that the recrystallization cannot be completed as expected by Avrami model.[42] In addition, the equilibrium phases (η) are continuously distributed along the grain boundaries and inside the grains. Figure 2(b) also displays the Al_3Zr particles that are distributed closely as white spots in SEM images. Features of this scale have significant influence on the recrystallization manner in AA7050.[41] We see that these dispersoids will have an influence on the recrystallization kinetics; in that sense, the recrystallization will be delayed and in extreme cases entirely inhibited. Instead, PFZ can be present at the vicinity of grain boundaries, or around second-phase particles upon the quenching stage.[43] The width and morphology of precipitated-free zones are highly affected by the processing conditions.[44] Figures 2(c) and (d) illustrates a precipitate-free zone of the 7050 aluminum alloy around the coarse-precipitated particles. Due to depletion of Zener pinning particles in the PFZ area, the mobility and migration of grain boundaries of recrystallizing grains are expected to be faster.[45]

D. Heterogeneous Distribution of the Recrystallization Pressure

As aforementioned, the constituent particles are insoluble intermetallic compounds of Mg_2Si and Fe-rich that form during ingot solidification.[4,8] Using imageJ software, the size of these large particles was found in the range of 1 to 55 μm.[4,8,46] During the hot-rolling process, these second-phase particles will affect the deformation microstructure and texture through effects such as an increase in dislocation density and the production of large deformation heterogeneities at larger particles.[10,47] The size and shape of the particle deformation zone (PDZ) depend on the particle size and the deformation mode.[10] During deformation, the PDZs were expected to elongate and overlap in the direction of rolling.[10,43] Qualitatively, the PDZs shape

was inferred from bright TEM micrographs (Figures 3(a) and (b)), to be an elongated oval.[10] The distribution and size of these deformation zones were associated to the large particles in BSE images.

During the static recrystallization, growth of the subgrains in AA7050 is controlled by two conflicting pressures, the driving pressure for growth (P_d), due to the dislocation density (ρ) or stored energy (E_D) accumulation around the large particle, and the Zener pinning pressure (P_z) arising from the dragging of finely random-dispersed particles (in terms of volume fraction and particle radius).[47] The net driving pressure for recrystallization (P) is thus $P = (P_d - P_z)$.[47] In this work, the Gibbs–Thompson Eq. [1] has been used to determine the critical particle size d_g for the nucleation of a recrystallized grain in terms of grain boundary γ_{GB}, energy between the nucleus and the deformation matrix, and the effective driving pressure for recrystallization ($P_D - P_Z$).[47,48]

$$d_g = 4\gamma_{GB}/(P_D - P_Z),$$
$$(P_D - P_Z) = 4\gamma_{GB}/d_g. \qquad [1]$$

In this project, the critical size d_g is the minimum particle size in which PSN of recrystallization can takes place which is 4 μm. On one hand, the subgrain boundary energy γ_{GB} was assumed to be measured by the Read–Shockley relation $J_{RS} = J_o \frac{\theta}{\theta_m}\left\{1 - \ln\left(\frac{\theta}{\theta_m}\right)\right\}$. The equation of the effective driving pressure can be rewritten in the following formula.

$$(P_D - P_Z) = 4J_{RS}\,(mJ\,m^{-2})/4\,(\mu m). \qquad [2]$$

The misorientation between subgrain with partial high-angle boundaries and deformed matrix is assumed to be large enough so that the grain boundary energy equals the maximum grain boundary energy of the simulation which is $J_{max} = 1$.[49] In the present study, the minimum critical size particle is considered to be 4 μm. Hence, the Eq. [2] will provide positive value driving

pressure for recrystallization particles equal or greater than to 1.

$$(P_D - P_Z) = \frac{4 * 1}{4} = 1. \qquad [3]$$

On the other hand, the interior regions within the grains are relatively free from large particles and so no recrystallized nuclei will be observed. In this case, Zener pinning pressure P_Z is assumed to be dominate due to the abundance of dispersoids inside the grains as observed from the TEM and SEM micrographs, Figure 2. As a result, the recrystallization is hindered, and the effective driving pressure for recrystallization is assumed to be negative or zero.

$$(P_D - P_Z) \le 0. \qquad [4]$$

Thus, in the current Monte Carlo algorithm for recrystallization, the recrystallizing subgrains will be able to grow if and only if the effective driving pressure for recrystallization $(P_D - P_Z)$ is positive and equals to unity, and no recrystallization will occur wherever $(P_D - P_Z)$ is assigned to be negative or zero in the areas far away from large particles and PDZs.

III. SIMULATION DEVELOPMENT

A. *Monte Carlo Potts Model*

In the current work, the initial microstructures for hot-rolled AA7050 alloy were characterized using EBSD obtained in a scanning electron microscope and analyzed using orientation imaging software (OIM). The Monte Carlo model is used for simulation of recrystallization and grain growth for a period of 500 Monte Carlo Step time in a domain size of 268×266 for sites on the RD-ND plane as well as 352×344 for the RD-TD plane sites. The total system energy is described by the Hamiltonian Eq. [5]. Every site contributes bulk energy, $(P_D - P_Z)(s_i)$ to the system in the recrystallization modeling. The external summation is on all N sites in the system, whereas the internal summation is on the nearest neighbor surface energy representing the total system energy. In Eq. [5], S_i and S_j are the old and new (randomly selected) spins, respectively; K is the Boltzmann constant, and T is the simulation temperature. Unlike the physical temperature, the temperature in the context of the Monte Carlo model governs the degree of disorder in the lattice. The lattice temperature (kT) is mostly set to 0.2–0.3 in order to maintain boundary roughness and to avoid lattice pinning effects.[50] One Monte Carlo time step (1 MCS) is defined as N reorientations where each of the N sites is given an opportunity to change orientation.[49–51]

The Read–Shockley model was employed in order to include the realistic textures and disorientation distributions in the Monte Carlo Potts algorithm. The Read–Shockley expression was implemented to depict the grain boundary energy, which varies at small disorientations (less than 15 deg).[20] Incorporating

anisotropy in the Monte Carlo approach requires an orientation identifier for each lattice site to be introduced. Hence, each lattice site was allocated with a spin identifier, S_i and an orientation identifier, O_i.[49]

$$E = \sum_{i=1}^{N} \sum_{J=1}^{z} \gamma(S_i, S_j, O_i, O_j) + \sum_i (P_D - P_Z)_i. \qquad [5]$$

The given Read–Shockley Eq. [6] was used in the Monte Carlo algorithm.[50]

$$J_{RS} = J_o \frac{\theta}{\theta_m} \left\{ 1 - \ln\left(\frac{\theta}{\theta_m}\right) \right\}, \qquad [6]$$

where θ_m is the maximum disorientation angle; it is reported that θ_m lie within 10 to 30 deg. In this work, θ_m is ordered of 15 deg.[49–53]

$$\gamma(S_i, S_j, O_i, O_j) = \begin{cases} 0 & \text{in the grain interios} (S_i = S_j, O_i = O_j) \\ \frac{J_{RS}}{2} & \text{for the boundaries } (S_i \ne S_j, O_i \ne O_j) \end{cases}. \qquad [7]$$

The mobility of grain boundaries was presumed to be a function of disorientation as well. Equation [6] was used by Okuda and Rollet for modeling recrystallization in elongated grains.[49]

$$M(S_i, S_j, O_i, O_j) = 1 - \exp\left\{ -0.5\left(\frac{\theta}{\theta_m}\right)^4 \right\}. \qquad [8]$$

The evolution of the structure was modeled by choosing a site from the recrystallizing subgrains that inserted at time zero of simulation in EBSD map according to the large particle distribution in BSE image. The new orientation from the set of allowable values was assigned at random for the recrystallizing grains.[52] The total system energy change, ΔE, for re-flipping the site is calculated, and the re-flipping was executed with transition probability [9].

$$P(S_i, S_j, \Delta E, T) = \begin{cases} \frac{J(S_i, S_j, O_i, O_j)}{J_{max}} \frac{M(S_i, S_j, O_i, O_j)}{M_{max}} & \Delta E \le 0 \\ \frac{J(S_i, S_j, O_i, O_j)}{J_{max}} \frac{M(S_i, S_j, O_i, O_j)}{M_{max}} \exp\left(\frac{-\Delta E}{kT}\right) & \Delta E > 0 \end{cases}, \qquad [9]$$

where J_{max} and M_{max} are the maximum boundary energy and the maximum mobility in the system, respectively, in this simulation we use $J_{max} = 1$ and $M_{max} = 1$.[49,52]

IV. RESULTS AND DISCUSSION

Figure 4, a BSE image shows the constituent large particles distributed along the grain boundaries elongated along the rolling direction (RD) and compressed along ND. Using imageJ software, the size of these large particles was found in the range of 1 to 55 μm. Figure 5 shows a large particle extended in the direction of rolling surrounded by multiple large equiaxed subgrains with
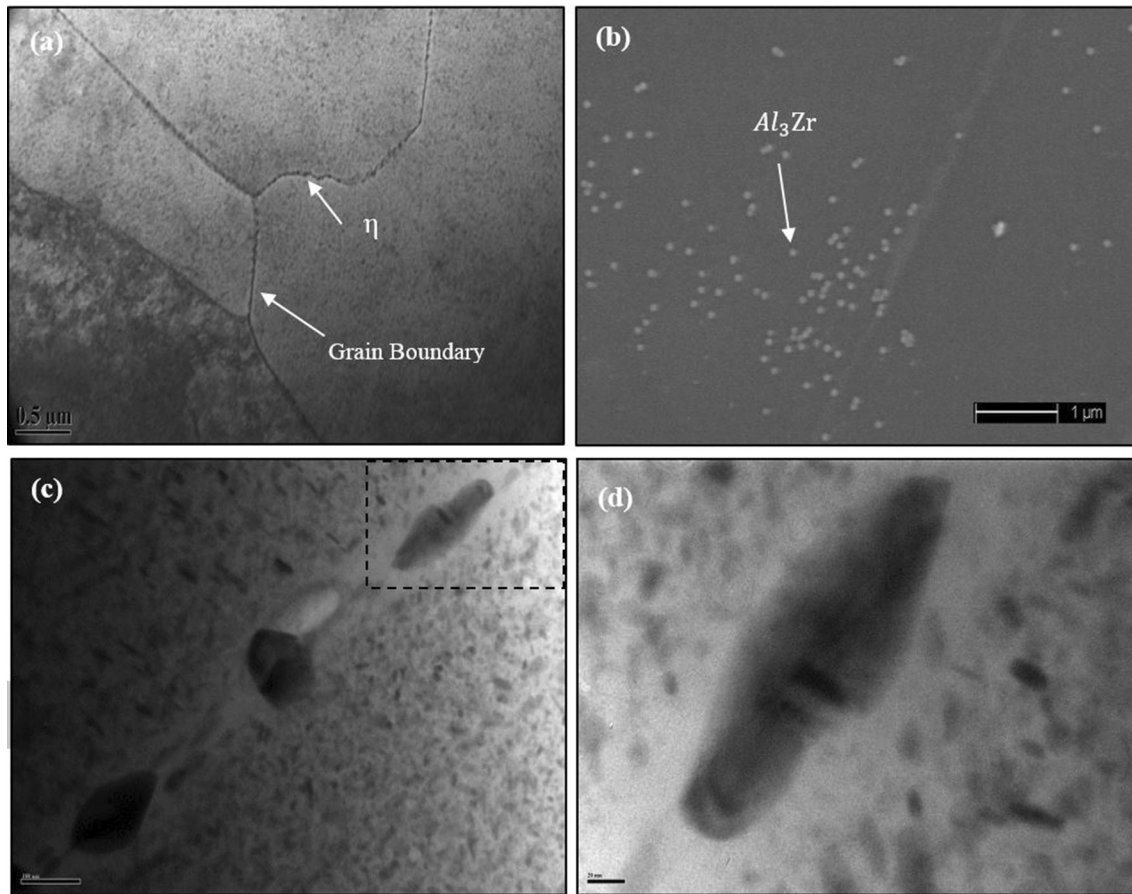
Fig. 2—Bright TEM microimages of 7050 aluminum alloy. (a) Distribution of nano-scale particles randomly in the matrix, in addition to hardening precipitate, η is banded on the grain boundaries. (b) SEM image illustrates that Al₃Zr particles are distributed closely as white spots, (c) and (d) precipitate-free zone around the coarse particles.
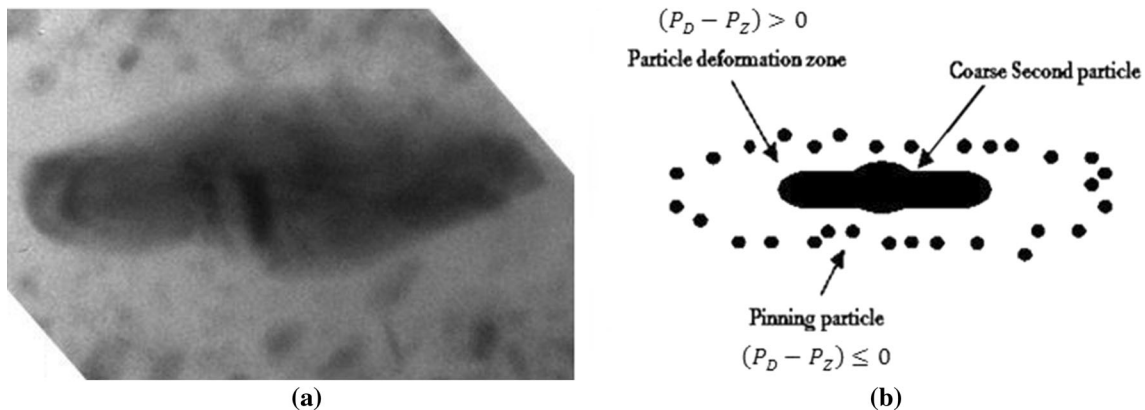

Fig. 3—Schematic diagram of (a) an actual pining depleted zone around a large particle, (b) extrapolated diagram for pining depleted zone around a large particle used in this simulation.

disparate orientations. These subgrains with partial high-angle grain boundaries (HAGBs) may act as nuclei during recrystallization as will be seen later.[54] Due to the degree of deformation (75 pct reduction) and the hot deformation temperature, the dislocations in the PDZ are able to recover and to form subgrains in the matrix close to the particles during the hot-rolling process.[55]

Figures 6(a) and (b) shows an orientation map of PSN recrystallized grains in the RD-ND plane of AA7050 alloy annealed for one hour. Overlapping the stored energy at the large particles along the grain boundaries and the absence of Zener pinning and precipitation effect, the recrystallized grains migrate and grow in alignment with the RD. Figure 6(b), the
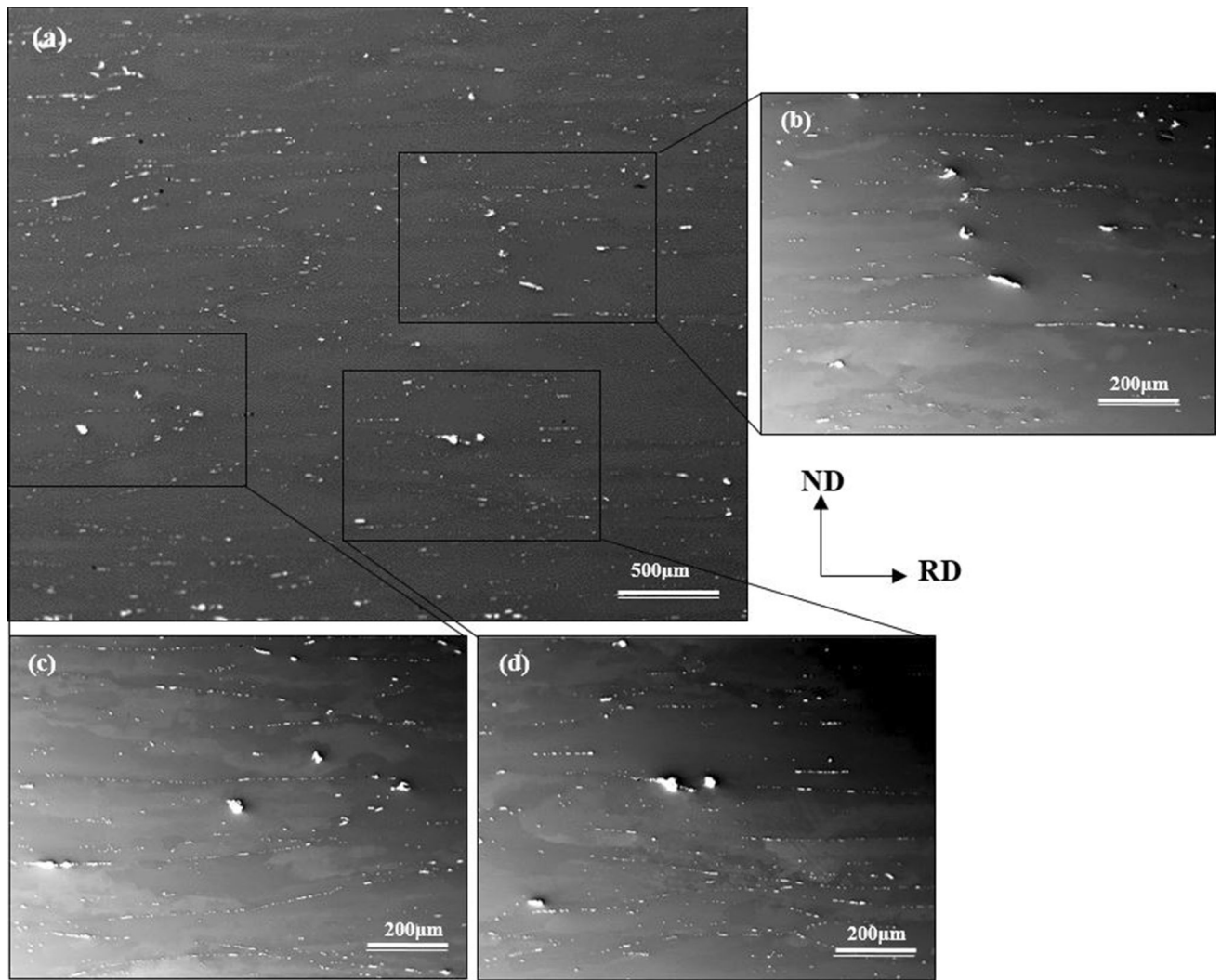
Fig. 4—Large particles distributed on the grain boundary in hot-rolled structure of AA7050, The microbar sizes are 500 μm for (*a*), and 200 μm for (*b* through *d*).

unrecrystallized regions are white and the recrystallized grains are identified to be dark, defined by grain orientation spread (GOS) of 1 or 2 degrees.[44,56] The elongated grain morphology is retained during recrystallization of these structures.[57]

Figures 7(a) through (c) provides further evidence that recrystallized structure resulting from PSN during EBSD *in situ* annealing of AA7050 for the same region at 573.15 K (300 °C). As it is clear from IQ image, the recrystallized grains are banded with sinusoidal boundaries in alignment with large particle distribution indicating that PSN is the dominant mechanism in the AA7050 alloy. As it is clear from Figure, the PSN takes place only at particles located along the grain boundaries, where the particles are slightly larger. The deformation heterogeneities around these large particles are often elongated in the direction of deformation. These regions which act as the preferred sites for nucleation of recrystallized grains during subsequent treatment.[10] The recrystallized grains grow and migrate in longitudinal patterns parallel to the RD in conjunction with the

coarse particle distribution. However, further precipitation is expected during later annealing. As will be shown later, the recrystallization sluggish at high annealing temperature during *in situ* heat stage annealing, it could be attributed to the effect of concurrent precipitation. Someday and Humphreys[58] have reported that recrystallizing elongated due to the precipitation pinning on the HAGBs and obstruct them from growth in the ND. Some of the individual recrystallizing grain orientations were extracted; these Euler angles of the recrystallized grains have been utilized for predicting the evolved texture in the simulation with tolerance ~10 deg.

A. *Simulated Microstructural Evolution*

A section parallel to the rolling plane and to the normal plane was chosen for the current study. Figures 8(a) and (b) displays the large particle distribution obtained by (BSE), together with the orientation map for the initial structure of hot-rolled AA7050 alloy of the same marked area of study obtained by EBSD.
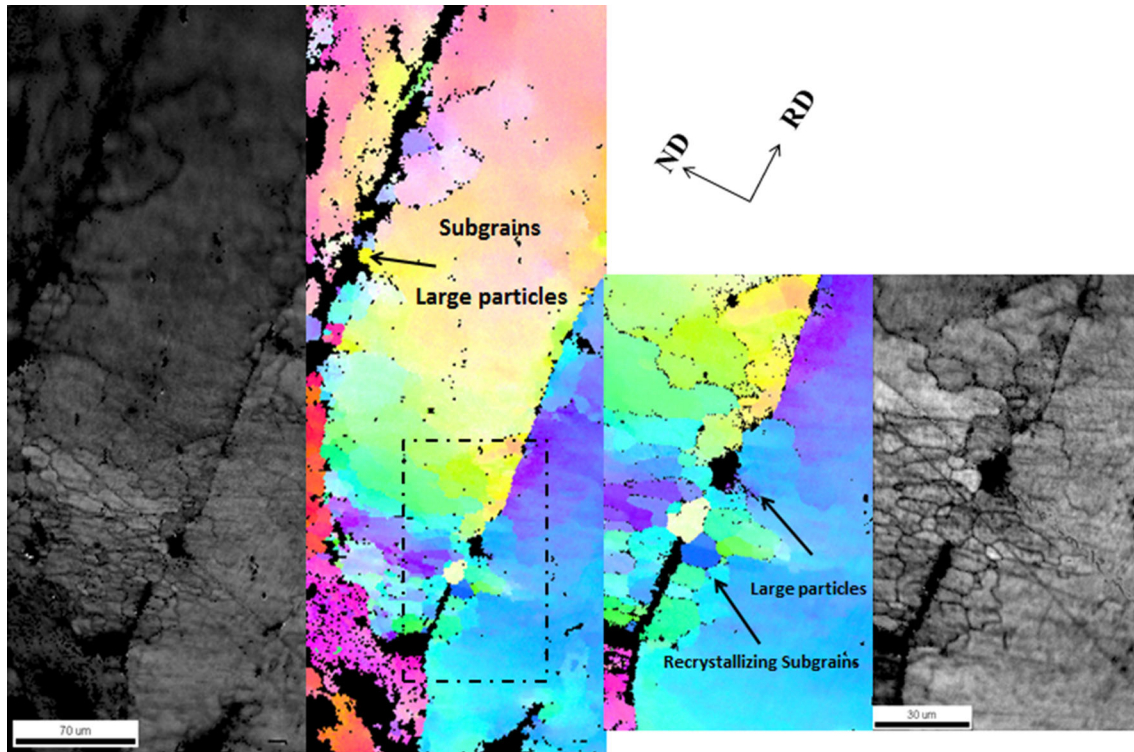
Fig. 5—EBSD IQ images and orientation maps showing the recrystallizing subgrains around the large particles for AA7050 structure during deformation, the micron bars are 70 and 30 μm. The orientation color keys are shown for poles aligned with the specimen normal direction.
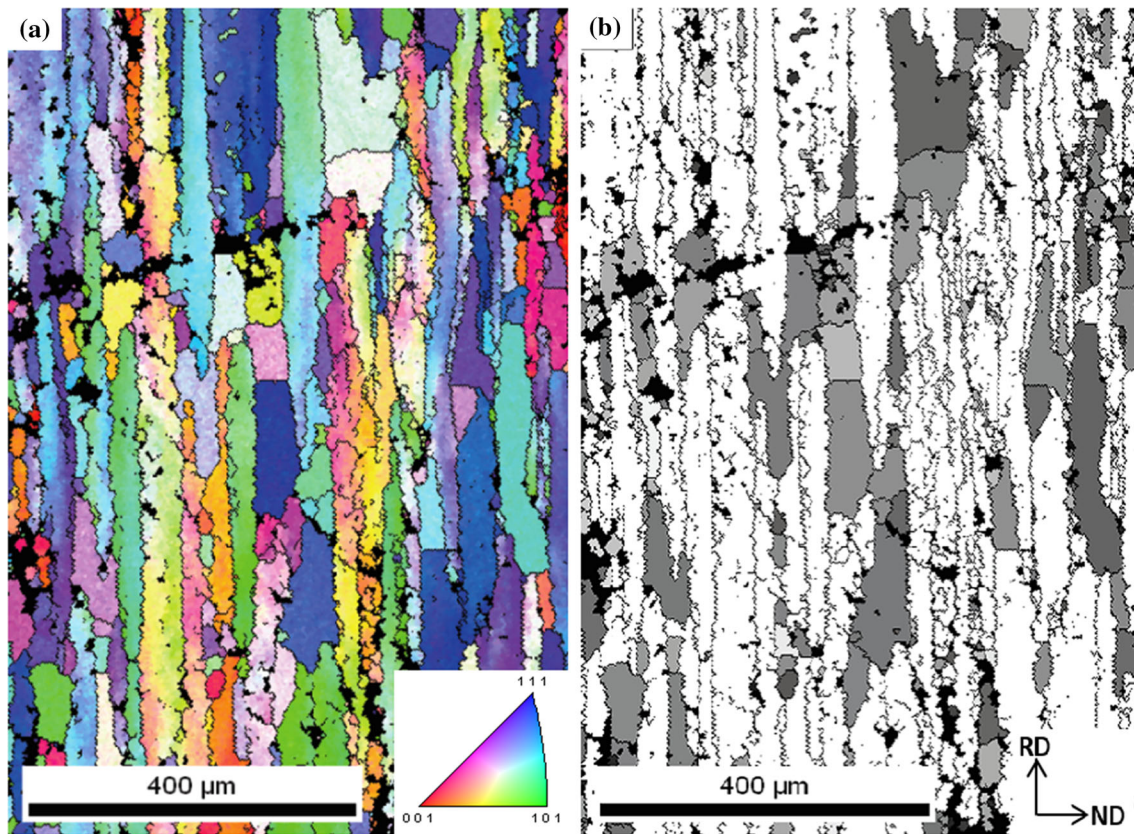

Fig. 6—Orientation map and recrystallized grains map for the 7050 alloy annealed for 60 min at 773.15 K (500 °C).

The observed variation in color (in the orientation map) arises from local variation in crystallographic orientation within grains caused by residual plastic strain. The coarse particles appear as black spots in a white matrix, they are aligned along the RD along the periphery of the flatted grains. The deformation heterogeneities, PDZ, are often found to be elongated in the direction of deformation, in conjunction with the coarse particle distribution. In regions of particle clustering, the PDZs overlap.[10] In this simulation, the particles of the order of 4 μm or greater were considered as critical size for a successful nucleation of a grain.[43,52] In addition, the spatial distribution of recrystallization driving pressure is related to that of large particles determined from the binarized BSE images. Yonghao Zhang and colleagues[19] have experimentally demonstrated to identify the nucleation sites during recrystallization the full 3D characterization is required. They found also that large nuclei and big particles extend over several microns beneath the surface which might lead to misinterpretations in 2D characterization (the number of nuclei might be less in the 2D characterization). To avoid this issue, a large quantity of recrystallized subgrains are inserted into the orientation map in the particle–matrix interface (and therefore the large number will be inserted around the large particle), according to their actual distribution in the BSE thresholded images with a range of orientation values dissimilar to non-recrystallized sets at the early stages of simulation (Figure 8(c)). The crystallographic orientation of these subgrains has been assigned to be random as it is observed from experimental data.

The predicted microstructural evolution during the recrystallization for the hot-rolled AA 7050 is summarized in Figures 8(c) through (i). At early time, the recrystallization driving pressure is high; the new strain-free PSN subgrains (with high grain boundaries) will rapidly grow to consume their neighbor subgrains before consuming the deformed or recovered microstructure.[51] The orientation maps at any time of simulation are divided into recrystallized or non-recrystallized regions, and the fraction recrystallized does not increase to 1 as the simulation proceeds, as shown in the PSN evolution sequence of Figure 8(c). The growth and migration of recrystallized grains in a longitudinal pattern is attributed to overlapping of the PDZs and the presence of precipitate-free zone around the grain boundaries and large particles. Compared with a single-phase alloy, recrystallization is hindered or even totally inhibited by pinning effect. After 40 MCS, time transition from accelerated to retarded recrystallization is clearly observed. The recrystallization grain growth will depend greatly on the particle distribution and size. The larger PSN subgrains dominate the recrystallized structure within the pinned structure. The evolved microstructure is partly recrystallized and the distribution of the recrystallized grains in the EBSD images match the distribution of coarse particles in the BSE images. The simulated microstructure qualitatively agrees with evolved structure of AA7050 from *ex-situ* annealing as shown in Figure 6.

To validate the modeling capability, a further computational attempt has been performed on the RD-TD
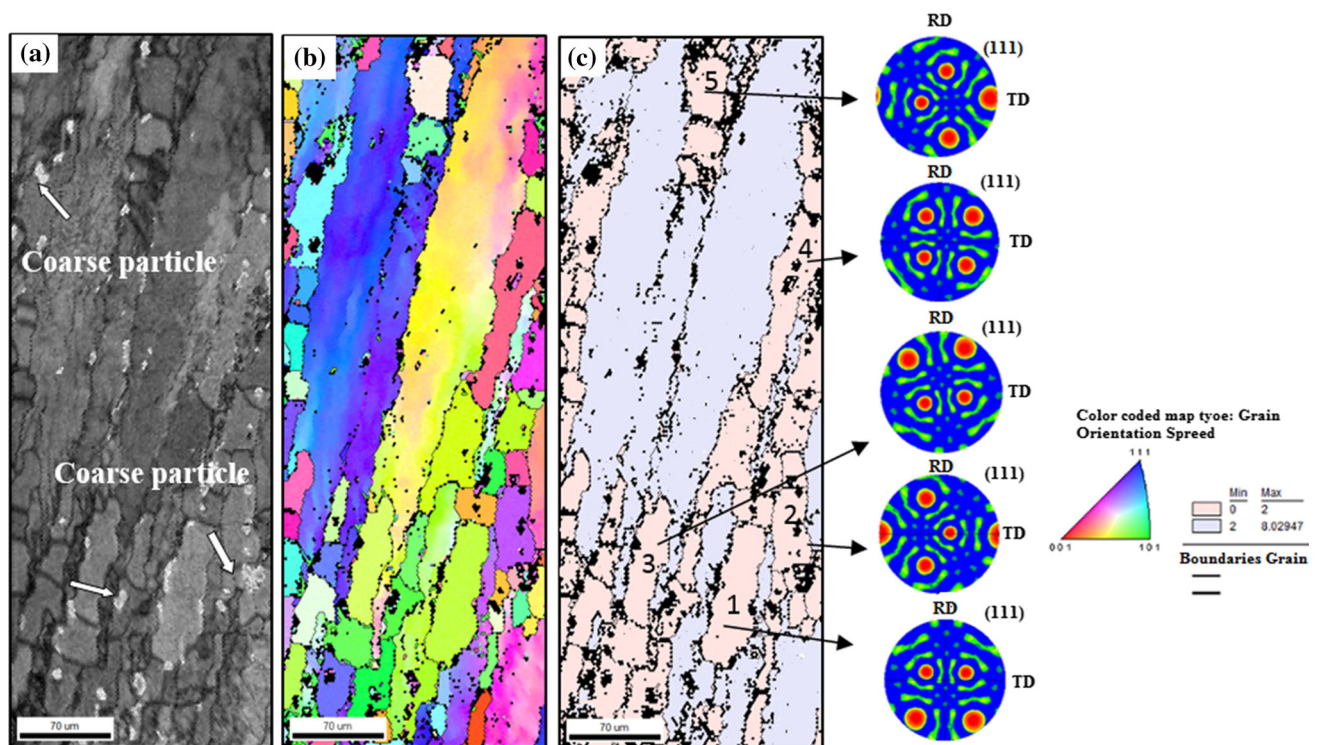

Fig. 7—EBSD Euler map of a region of the sample AA7050 at 573.15 K (300 °C), (*a*) IQ images shows the coarse particle distribution and recrystallized grains (*b*) the same region at 573.15 K (300 °C), (*c*) the pink color identifies PSN recrystallized grains defined by grain orientation spread (GOS) of 2 degree.

plane of the same sample as shown below in Figures 8(j) through (l). The initial and final microstructures of RD-TD plane beside the particle distribution are provided. Again the nucleation sites are non-randomly distributed. However, the anisotropic distribution of these particles is frequently in alignment with the rolling.

Clustering of recrystallizing subgrains grows at the periphery of the pancake deformed grains where the large particles are located forming a necklace shape. The decrease in the growth rate perpendicular to the RD results in pancake grains after recrystallization as clearly shown in Figure 8. Thus, the simulation model predicts
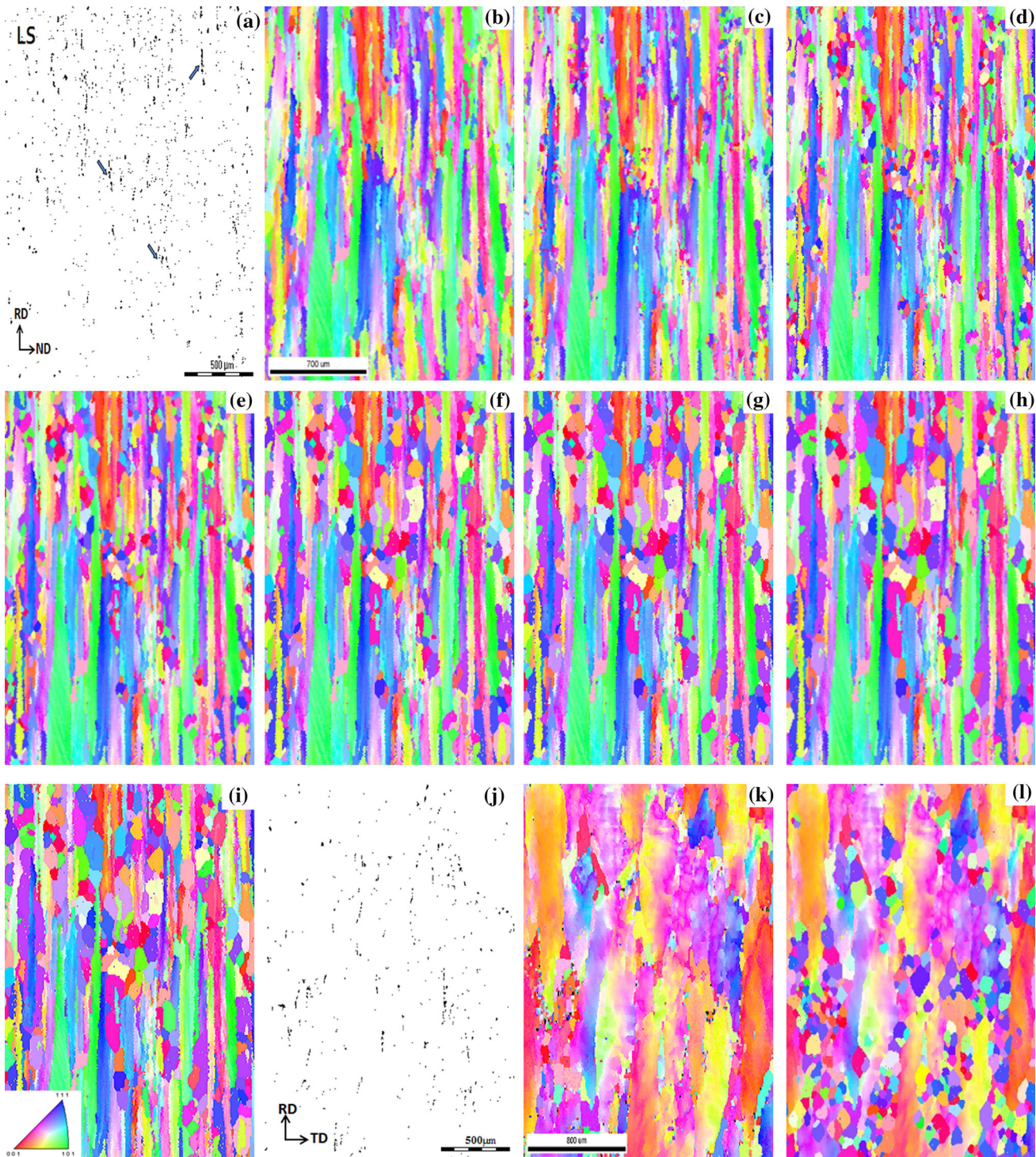

Fig. 8—RD-ND Plane for (*a*) through (*i*): (a) Binarized BSE images, (b) EBSD orientation map for initial microstructure of AA7050, Snapshots of simulation microstructure evolution during recrystallization using Pott's Monte Carlo Model, (c) at MCS = 10, (d) at MCS = 50, (e) at MCS = 250, (i) at MCS = 500. RD-TD Plane for (*j*) through (*l*): (j) Binarized BSE images, (k) EBSD orientation map for initial microstructure of AA7050, Snapshots of simulation microstructure evolution (d) at MCS = 500.
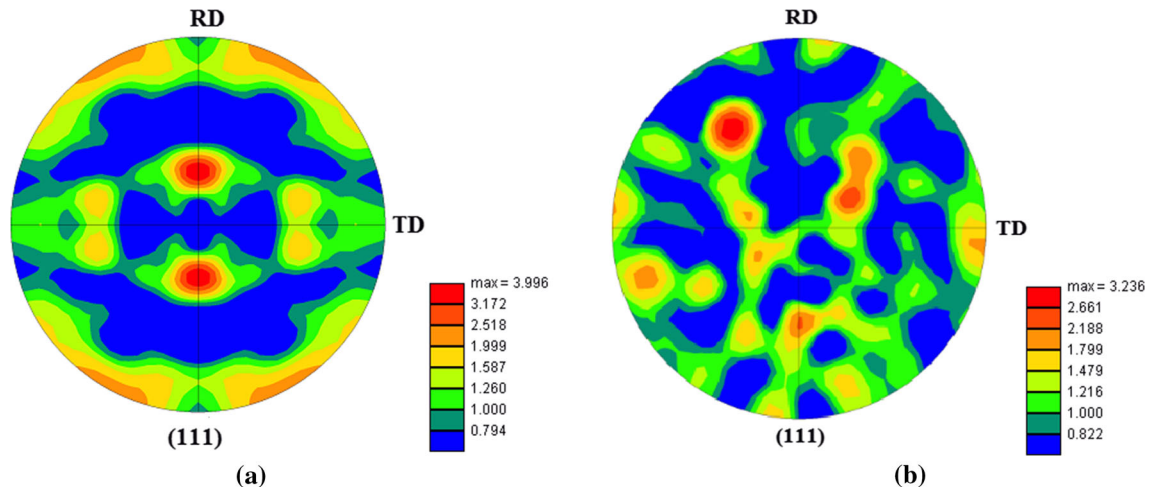
Fig. 9—(111) pole figures showing textures of (*a*) the deformed grains at time 0 MCS and (*b*) the modeled recrystallized grains orientation at time 500 MCS scale.
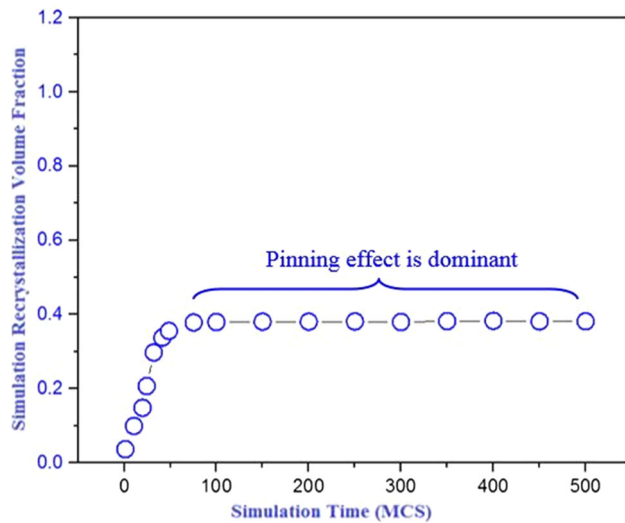

Fig. 10—Recrystallization kinetics obtained from Monte Carlo simulation results for the RD-ND plane.

accurately the microstructure during recrystallization which mainly occurs due to the PSN mechanism, and it also demonstrates that recrystallization fraction of this alloy can be optimized by controlling the large particles fraction prior to thermomechanical procedures.[10]

B. *Crystallographic Texture*

The prediction of textures developed during recrystallization is still poor unlike the deformed textures.[59] The effect of PSN on the recrystallization textures in 7050 Al alloys were evaluated by analyzing the micro-texture of subgrains in the deformation zones and the recrystallized subgrains. The nuclei are assumed to initiate inside the deformation zones, and therefore, their orientations will be constrained to those existing in these zones which are presumed to be random and weak.[47,59] In order to quantify the recrystallized texture

by means of OIM software, confidence indices are set to 1 for all recrystallized grains during the simulation. Figure 9 shows the textures using (111) pole figures for hot-rolled and simulated evolved structures for AA7050. The slight difference in texture of the hot-rolled structure from typical texture can be owed to deformation zone around the non-deformable particles. Figure 9(b) shows the randomness in orientations which is attributed to PSN of the recrystallized grains in of simulation RD-ND plane.[60–63]

C. *PSN Recrystallization Behavior*

A finite fraction of subgrains was assigned dependent on the coarse particles fraction in the matrix as site saturated nucleation conditions at the beginning of the MC simulations. As revealed in Figure 10, at early time of simulation, the recrystallizing subgrains growth will be initially rapid, but will decrease when these regions of high-stored energy are consumed. Afterward, the growth rate tends to be constrained by impingement of recrystallizing subgrains from their neighbors within the deformation zone, and then the recrystallization will be controlled by the surface energy of the recrystallizing subgrains. In comparison with the experiment, it is obvious to note that the recrystallization fraction for simulation does not match the Avrami exponent, and the recrystallization volume fraction does not increase as the simulation processed to 1. Due to depletion of the effective recrystallization pressure within the PDZ and dominating pinning pressure in the region far away from large particles, a small volume fraction of recrystallization is obtained.[47]

D. *In Situ Microstructural Evolution*

In situ performed using EBSD to present PSN static recrystallization occurring in hot-rolled 7050 aluminum alloy. The sequence of orientation maps from *in situ* heating of hot-rolled AA7050 and the texture at selected temperatures and times repressed using TSL OIM
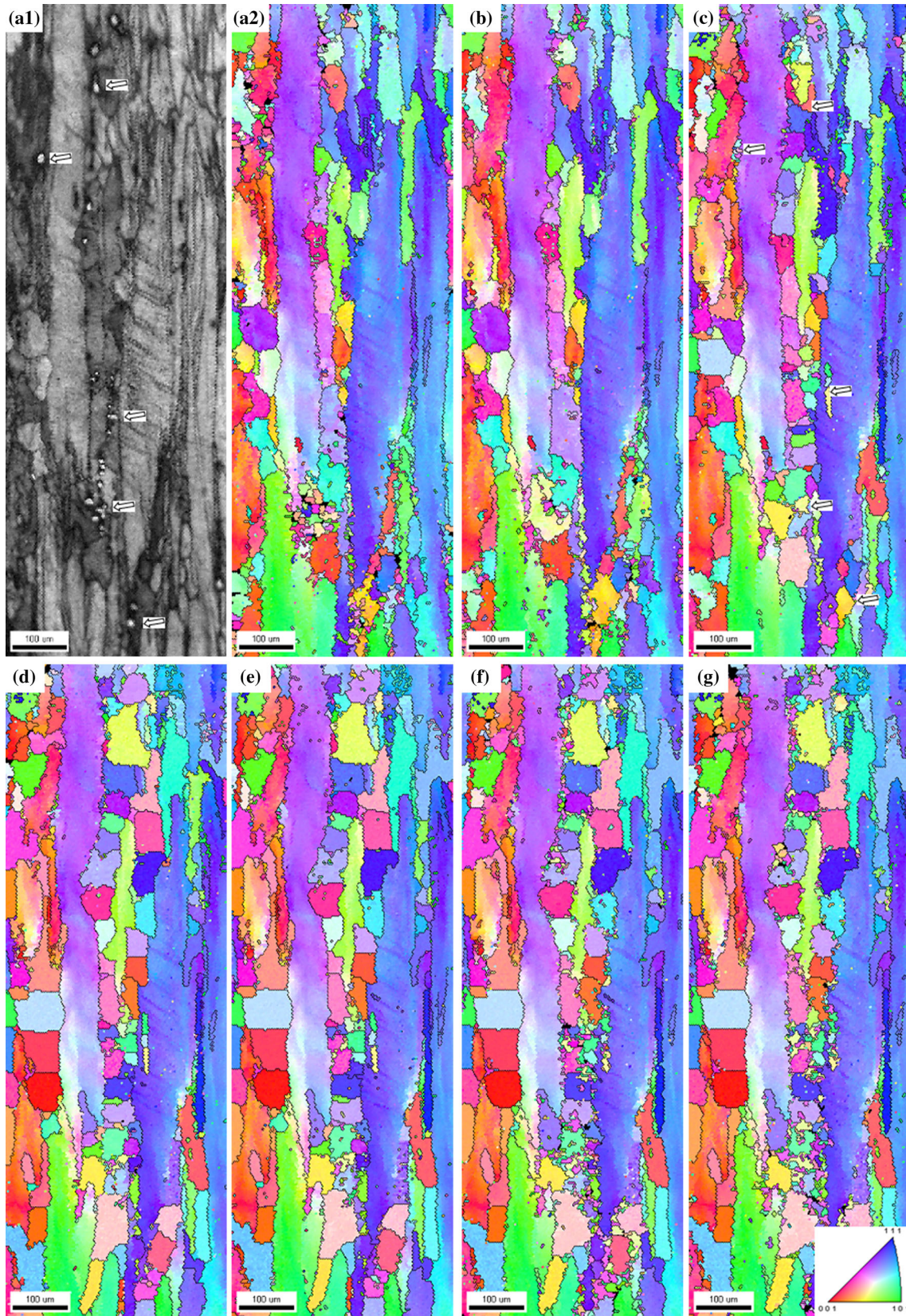
Fig. 11—Sequence of orientation maps from *in situ* heating of hot-rolled AA7050 alloy at selected times and temperatures (*a*) 0 min, 298.15 K (25 °C), (*b*) 60 min, 523.15 K (250 °C), (*c*) 65 min, 548.15 K (275 °C), (*d*) 70 min, 573.15 K (300 °C), (*e*) 80 min, 598.15 K (325 °C), (*f*) 90 min, 623.15 K (350 °C), (*g*) 140 min, 623.15 K (350 °C).
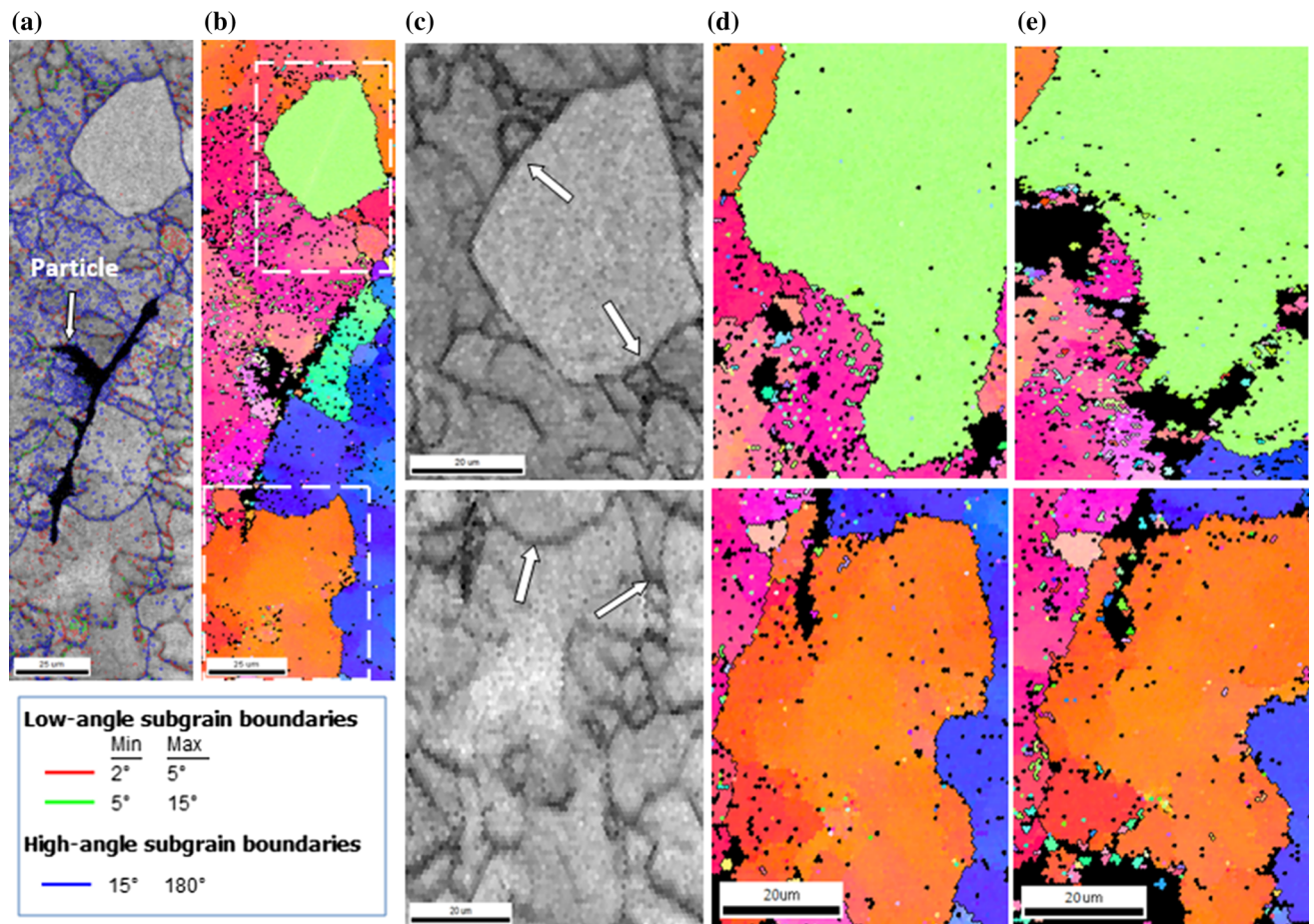
Fig. 12—Orientation maps for AA7050 obtained by automated EBSD analyses. Orientation mapping was performed during *in situ* heating in region adjacent to large particle; before heating (*a*) and (*b*), (a) Grain boundary map, (b) Orientation map of initial microstructure, (*c*) white arrow indicates to propagation of subgrain boundary (arrowed) along with migrating boundary, (*d*) 598.15 K (325 °C), (*e*) 623.15 K (350 °C).

Analysis 6 software by imposing the Orthotropic (Rolled sheet) symmetry.[64] The observed evolution is related to holding temperature and time during *in situ* annealing. As it is pointed to by arrows, the large particles are white spots and pre-existing subgrain within the deformation zone are darker regions (Figure 11(a1)). Figure 11(b) shows the orientation map at 523.15 K (250 °C) and no microstructural change is noticed at temperature 523.15 K (250 °C) compared with the snap shot for the initial microstructure at room temperature (Figure 11(a2)). As the temperature increases to 548.15 K (275 °C), a group of new recrystallized grains is clearly observed and related to pre-existing second-phase particles in Figure 11(c). This indicates that the recrystallizing subgrains arise favorably near the second-phase particles. In the other words, recrystallization initiates at a pre-existing subgrain in the deformation zone, around the particle surface. As *in situ* annealing continues, it can be noted that recrystallizing subgrains grow and some vanish and are replaced with other subgrains nucleated just below the surface. The developments in the recrystallized microstructures do not only confirm the nucleation and growth of the recrystallized grains that have heterogeneous character but also confirm that lack of precipitation and Al_3Zr particles near the grain boundaries contribute to the fast recrystallization at the subgrains along the grain boundaries. This results in growth of the recrystallized grains parallel to the RD which match the simulation results. Afterward, the recrystallization grain growth is driven by the surface energy or the grain boundary energy within the pinned grains structure and the growth rate diminishes as recrystallization proceeds and the larger PSN subgrains dominate the recrystallized structure. Later at 573.15 K (300 °C) to 623.15 K (350 °C), Figures 11(f) through (g) after 80 minutes, the grain structure stabilized and no further evolution was observed after annealing for 60 minutes at 623.15 K (350 °C). This recrystallization sluggish at high annealing temperature might be attributed to pinning particles arising from concurrent precipitation beside the zirconium particles effect.

E. *Growth of Recrystallizing Subgrains*

Recrystallized subgrains were identified as those being comparatively or entirely surrounded by a high-angle boundary (>15 deg) with inner misorientations less than 2 deg Figure 12(a). Pre-existing low- and high-angle boundaries in the area close to large particles with

diverse misorientation intervals are presented as colored lines on the orientation maps in Figure 12(a). During the early heating in the SEM subgrain boundaries, inside individual grains rearranged and moved and the misorientation angle of pre-existing subgrain boundaries increased, as the temperature increased some new ones developed and some subgrain boundaries disappear. The grain boundaries migration of these subgrains in the deformed zone is essentially driven due to differences in the stored strain energy carried by dislocation.[65] The arrow pointed to the moving boundary of high-angle boundary of the recrystallizing subgrains (misorientation angle >15 deg) which are expected to have higher mobility than other grain boundaries and, therefore, grow at the expense of neighboring subgrains Figures 12(d) through (f).

F. Recrystallization Texture

The recrystallization texture of the evolved microstructures from *in situ* EBSD annealing was also examined. The (111) pole figure was used to track the orientational change during *in situ* annealing. The initial texture 298.15 K (25 °C) is a typical (fcc) rolling texture (see Figure 13(a)), some of the deformation components such as brass, S, and Cu are present in the initial texture. Upon heating above 523 K (250 °C), the PSN subgrains

activate and as the *in situ* annealing progresses, the weak and deviation from the typical rolling orientation start appearing in Figures 13(c) through (f)).

Figure 14 shows the GOS for scan plotted as a function of temperature and time. Figures 14(a) and (b) show the histograms of these data with the relative intensities of each GOS value plotted for a deformed structure and a partially recrystallized structure. Figure 14(b) shows a somewhat bi-modal distribution, as expected, whereas it is apparent that the recrystallized and unrecrystallized regions are not well-separated in this alloy by the GOS measure. However, as it would be expected, the GOS declines as recrystallization continues in the specimen. This indicates how recrystallized grains are consuming the deformed regions in the microstructure.

V. SUMMARY AND CONCLUSIONS

The PSN of recrystallization for high-strength 7050 Al alloys was simulated on a mesoscale level by utilizing the Monte Carlo Potts model. The actual microstructure and particle distribution of hot-rolled plate were emphasized as an initial point for modeling of recrystallization. Compared with the published works that incorporate a theoretical nuclei site distribution as input, here the nucleation sites were determined from a set of
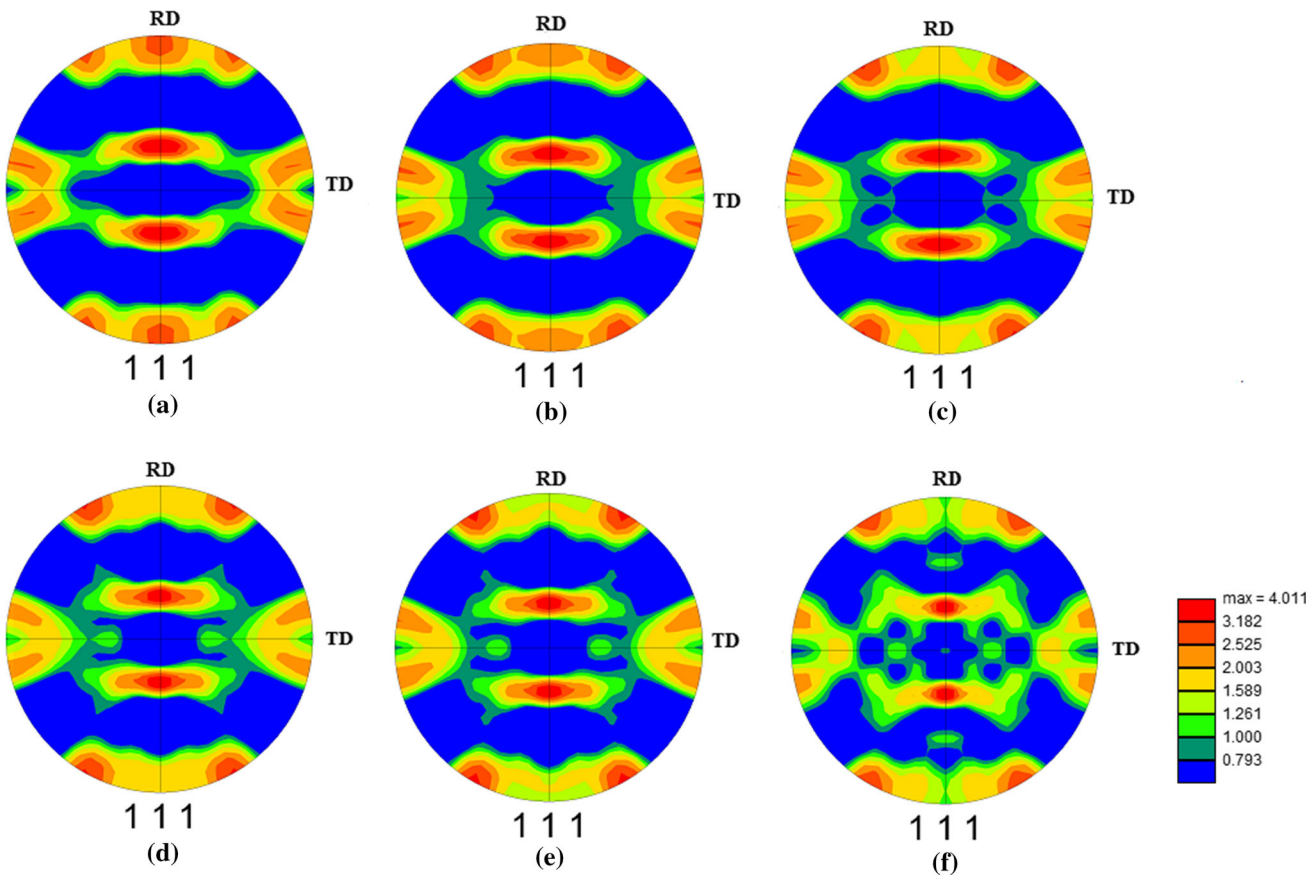

Fig. 13—(111) Pole figures of evolved orientation maps from *in situ* heating of hot rolled AA7050 alloy at selected times and temperatures (*a*) 298.15 K (25 °C), (*b*) 523.15 K (250 °C), (*c*) 548.15 K (275 °C), (*d*) 573.15 K (300 °C), (*e*) 598.15 K (325 °C), (*f*) 623.15 K (350 °C).
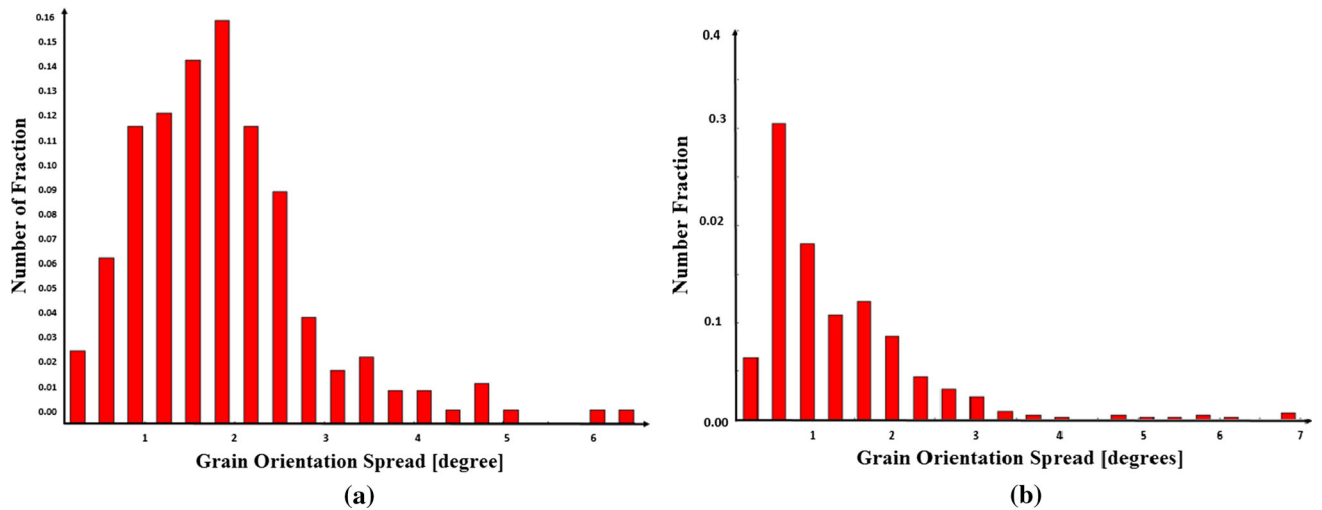
(a)

(b)

Fig. 14—GOS histograms showing representative distributions for (*a*) hot-rolled AA7050 at 0 min and room temperature (*b*) at 140 min annealed at 623.15 K (350 °C).

experimentally acquired BSE micrographs and used as model inputs. The effective recrystallization pressure $(P_D - P_Z)$ distribution was related to the large distribution. Precipitate-free zones around grain boundaries and coarse particles were depicted in TEM micrographs. In order to model the PSN recrystallization, a positive driving pressure was assigned around the coarse particles, and a negative pressure was assigned for sites far away from the coarse particles in the matrix. The simulated grain structure showed very good agreement with the recrystallized structure of experimental data, and the recrystallization in this alloy was shown to be dominated by PSN. The growth and migration of recrystallized grains in a longitudinal pattern is attributed to overlapping of the PDZs, and the presence of precipitate-free zone around the grain boundaries and large particles are witnessed in both simulation and experimental rustles. The subsequent grain growth is driven by the surface energy within the pinned grains structure and the growth rate diminishes as recrystallization proceeds. The randomness and weakness in the texture of the simulated recrystallized grains are induced from the recrystallization texture of the experimental data obtained from EBSD. Moreover, *In situ* EBSD experiments have performed to verify the validity of simulation results and elucidating that PSN is the dominant mechanism of recrystallization in AA7050 alloy. The evolved microstructure from *in situ* annealing confirmed the nucleation and growth of the recrystallized grains has heterogeneous character.

REFERENCES

1. J.D. Robson: *Mater. Sci. Eng. A*, 2004, vol. 382, pp. 112–21.
2. J.T. Staley and D.J. Lege: *J. De Phys. IV*, 1993, vol. 3, pp. 179–90.
3. D. Dumont, A. Deschamps, and Y. Brechet: *Mater. Sci. Eng. A*, 2003, vol. 365, pp. 326–36.
4. D.P. Field, L. Behrens, and J.M. Root: *Tech Sci. Press*, 2009, vol. 14 (3), pp. 171–83.
5. S.F. Harnish, H.A. Padilla, J.A. Dantzig, A.J. Beaudoin, B.E. Gore, I.M. Robertson, and H. Weiland: *Metall. Mater. Trans. A.*, 2005, vol. 36A (2), pp. 357–69.
6. Y.L. Deng, L. Wan, Y. Zhang, and X.-M. Zhang: *J. Alloy. Compd.*, 2010, vol. 488, pp. 88–94.
7. Root, J. M. M.: Master Dissertation, Pullman, Wash, Washington State University, 2010.
8. I.J. Polmear: *Light Alloys from Traditional Alloys to Nanocrystals*, 4th ed., Elsevier, Oxford, 2006, pp. 29–96.
9. B. Radhakrishnan and G.B. Sarma: *Continuum Scale Simulation of Engineering Materials Fundamentals—Microstructures—Process Applications*, Wiley, Weinheim, 2004, pp. 343–59.
10. R. Doherty, D. Hughes, F. Humphreys, J. Jonas, D. Jensen, M. Kassner, W. King, T. Mcnelley, H. Mcqueen, and A. Rollett: *Mater. Sci. Eng.*, 1997, vol. 238, pp. 219–74.
11. B. Radhakrishnan and G. Sarma: *Philos. Mag.*, 2004, vol. 84 (22), pp. 2341–66.
12. S. Storm and D.J. Jensen: *Scripta Mater.*, 2009, vol. 60 (7), pp. 477–80.
13. B. Brahme, J. Fridy, H. Weiland, and A.D. Rollett: *Modell. Simul. Mater. Sci. Eng.*, 2009, vol. 17, p. 015005.
14. E.A. Holm, M.A. Miodownik, and A.D. Rollett: *Acta Mater.*, 2003, vol. 51 (9), pp. 2701–16.
15. J.D. Robson and P.B. Prangnell: *Act Mater.*, 2001, vol. 49, pp. 599–613.
16. W.R. Yancy and T.H. Sanders, Jr: *Mater. Sci. Forum*, 2000, vols. 331–337, pp. 799–804.
17. H. Weiland and S.W. Cheong: *Mater. Sci. Forum*, 2007, vols. 558–559, pp. 383–87.
18. Eivani, A. Z., Zhou, J., and Duszczyk, J.: *Recent Trends in Processing and Degradation of Aluminum Alloys*, InTech, 2011, pp. 477–515.
19. K. Huang, O. Engler, Y.J. Li, and K. Marthinsen: *Mater. Sci. Eng. A*, 2015, vol. 628, pp. 216–29.
20. W. Xu, M. Ferry, J. Cairney, and F. Humphreys: *Acta Mater.*, 2007, vol. 55, pp. 5157–67.
21. J.D. Robson, D.T. Henry, and B. Davis: *Acta Mater.*, 2009, vol. 57, pp. 2739–747.
22. T.A. Bennett, R.H. Petrov, L.A.I. Kestens, L.Z. Zhuang, and P. De Smet: *Scripta Mater.*, 2010, vol. 63, pp. 461–64.
23. Y. Zhang, D.J. Jensen, Y. Zhang, F. Lin, Z. Zhang, and Q. Liu: *Scripta Mater.*, 2012, vol. 67, pp. 320–23.
24. L.P. Troeger and E.A. Starke: *Mater. Sci. Eng. A*, 2000, vol. A293, pp. 19–29.
25. C.S. Ramesh, R. Keshavamurthy, P.G. Koppad, and K.T. Kashyap: *Trans. Nonferrous Met. Soc. China*, 2013, vol. 23, pp. 53–58.
26. X. Song and M. Rettenmay: *Comput. Mater. Sci.*, 2007, vol. 40 (2), pp. 234–45.
27. A.R. Eivani, J. Zhou, and J. Duszczyk: *Comput. Mater. Sci.*, 2014, vol. 86, pp. 193–99.

28. F. Caleyo, T. Baudin, and R. Penelle: *Scripta Mater.*, 2002, vol. 46 (12), pp. 829–35.
29. T. Baudin, P. Paillard, and R. Penelle: *Scripta Mater.*, 1997, vol. 36 (7), pp. 789–94.
30. S.I. Wright: *Electron Backscatter Diffraction in Materials Science, 2Ed*, Springer Science, New York, 2009, pp. 329–37.
31. A. Lens, C. Maurice, and J.H. Driver: *Mater. Sci. Eng.*, 2005, vol. A403 (1), pp. 2144–53.
32. D.P. Field, L. Bradford, M. Nowell, and T. Lillo: *Acta Mater.*, 2007, vol. 55 (12), pp. 4233–241.
33. Nowell, M. M., Field, D. P., Wright, S. I., Dingley, D., Scutts, P., and Suzuki, S.: *Microscopy and Microanalysis*, 2005, MAM11.S02.
34. M.M. Nowell, S.I Wright, and J.O. Carpenter: *Microsc. Microanal.*, 2009, vol. 15 (S2), pp. 678–79.
35. S.L. Raghunathan, R.J. Dashwood, M. Jackson, S.C. Vogel, and D. Dye: *Mater. Sci. Eng. A*, 2008, vol. 488 (1–2), pp. 8–15.
36. K. Kajihara, K. Matsumoto, and K. Matsumoto: *Mater. Sci. Forum MSF*, 2006, vols. 519–521, pp. 1579–584.
37. P.J. Hurley and F.J. Humphreys: *J. Microsc.*, 2004, vol. 213 (3), pp. 225–34.
38. I. Lischewski, D.M. Kirch, A. Ziemons, and G. Gottstein: *Appl. Anal. Text.*, 2009, vol. 201, pp. 95–102.
39. D.P. Field: *Ultramicroscopy*, 1997, vol. 67 (1–4), pp. 1–9.
40. M.A. Groeber and M.A. Jackson: *Integr. Mater. Manuf. Innov.*, 2014, vol. 3 (5), pp. 1–17.
41. M.D. Abramoff, P.J. Magalhaes, and S.J. Ram: *Biophotonics Int.*, 2004, vol. 11 (7), pp. 36–42.
42. M. Avrami: *J. Chem. Phys.*, 1939, vol. 7, pp. 1103–12.
43. A. Deschamps: *Handbook of Aluminum Volume 2 Alloy Production and Materials Manufacturing*, Marcel Dekker, Inc, New York, 2003, pp. 47–80.
44. J.H. Cho, A.D. Rollett, J.S. Cho, Y.J. Park, J.T. Moon, and K.H. Oh: *Metall. Trans.*, 2006, vol. 37A, pp. 3085–97.
45. J.F. Chen, L. Zhen, J.T. Jiang, L. Yang, W.Z. Shao, and B.Y. Zhang: *Mater. Sci. Eng.*, 2012, vol. A539, pp. 115–23.
46. S. Tangen, K. Sjølstad, T. Furu, and E. Nes: *Metall. Mater. Trans. A*, 2010, vol. 41A (11), pp. 2970–83.
47. F.J. Humphreys and M. Hatherly: *Recrystallization and Related Annealing Phenomena*, 3rd ed., Elsevier Science Inc., Oxford, 1995, pp. 285–319.
48. H.E. Vatne and E. Nes: *Comput. Mater. Sci.*, 1996, vol. 7, pp. 5–10.
49. M. Miodownik: *Computational Materials Engineering an Introduction to Microstructure Evolution*, Elsevier Inc, Oxford, 2007, pp. 47–108.
50. K. Okuda and A.D. Rollett: *Comput. Mater. Sci.*, 2005, vol. 34, pp. 264–73.
51. D. Zöllner and P. Streitenberger: *Micro-Macro-Interactions in Structured Media and Particle Systems*, Springer, Chennai, 2008, pp. 3–18.
52. A.D. Rollett and P. Manohar: *Continuum Scale Simulation of Engineering Materials Fundamentals—Microstructures—Process Applications*, Wiley, Weinheim, 2004, pp. 77–111.
53. A.D. Rollett: *JOM*, 2004, vol. 56 (4), pp. 63–68.
54. R.D. Doherty: *Progress m Marerrals Scrence*, 1997, vol. 42, pp. 39–58.
55. O. Engler, X.W. Kong, and P. Yang: *Scripta Mater.*, 1997, vol. 37 (11), pp. 1665–74.
56. D.P. Field, L.T. Bradford, M.N. Nowell, and T.M. Lillo: *Acta Mater.*, 2007, vol. 55, pp. 4233–41.
57. C. Mondal, A.K. Singh, A.K. Mukhopadhyay, and K. Chattopadhyay: *Metall. Mater. Trans. A*, 2013, vol. A44 (6), pp. 2764–77.
58. M. Somerday and F.J. Humphreys: *Mater. Sci. Technol.*, 2003, vol. 19, pp. 20–29.
59. G. Gottstein and R. Sebald: *J. Mater. Process. Technol.*, 2001, vol. 117, pp. 282–87.
60. C. Schäfer, J. Song, and G. Gottstein: *Acta Mater.*, 2009, vol. 57 (4), pp. 1026–34.
61. R.A. Vandermeer and D.J. Jensen: *Acta Mater.*, 2003, vol. 51, pp. 3005–18.
62. F. Habiby and F.J. Humphreys: *Text. Microstruct.*, 1993, vol. 20, pp. 125–40.
63. B. Verlinden, J. Driver, I. Samajdar, and R.D. Doherty: *Thermo-mechanical Processing of Metallic Materials*, 1st ed., Elsevier, Amsterdam, 2007.
64. S.I. Wright and B.L. Adams: *Metall. Trans. A*, 1992, vol. 23, pp. 759–67.
65. M. Bestmann, S. Piazolo, C.J. Spiers, and D.J. Prior: *J. Struct. Geol.*, 2005, vol. 27 (3), pp. 447–57.